

MIT Open Access Articles

M13 Virus-Enabled Synthesis of Titanium Dioxide Nanowires for Tunable Mesoporous Semiconducting Networks

The MIT Faculty has made this article openly available. **Please share** how this access benefits you. Your story matters.

Citation: Chen, Po-Yen, Xiangnan Dang, Matthew T. Klug, Noémie-Manuelle Dorval Courchesne, Jifa Qi, Md Nasim Hyder, Angela M. Belcher, and Paula T. Hammond. "M13 Virus-Enabled Synthesis of Titanium Dioxide Nanowires for Tunable Mesoporous Semiconducting Networks." *Chemistry of Materials* 27, no. 5 (March 10, 2015): 1531–40.

As Published: <http://dx.doi.org/10.1021/cm503803u>

Publisher: American Chemical Society (ACS)

Persistent URL: <http://hdl.handle.net/1721.1/102442>

Version: Original manuscript: author's manuscript prior to formal peer review

Terms of Use: Article is made available in accordance with the publisher's policy and may be subject to US copyright law. Please refer to the publisher's site for terms of use.



M13 Virus-Enabled Synthesis of Titanium Dioxide Nanowires for Mesoporous Semiconducting Networks

Po-Yen Chen^{†,§}, Xiangnan Dang^{§,‡}, Matthew T. Klug^{§,1}, Noémie-Manuelle D. Courchesne^{†,§}, Jifa Qi^{§,‡}, Md Nasim Hyder^{†,§}, Angela M. Belcher^{§,‡,±,}, Paula T. Hammond^{†,§,*}*

[†]Department of Chemical Engineering, Massachusetts Institute of Technology,
Cambridge, MA 02139 (USA)

[§]The David H. Koch Institute for Integrative Cancer Research, Massachusetts Institute of
Technology, Cambridge, MA 02139 (USA)

[‡]Department of Materials Science and Engineering, Massachusetts Institute of
Technology, Cambridge, MA 02139 (USA)

¹Department of Mechanical Engineering, Massachusetts Institute of Technology,
Cambridge, MA 02139 (USA)

[±]Department of Biological Engineering, Massachusetts Institute of Technology,
Cambridge, MA 02139 (USA)

* Address correspondence to belcher@mit.edu and hammond@mit.edu

ABSTRACT

Mesoporous semiconducting networks exhibit advantageous photo-electrochemical properties. The M13 virus is a versatile biological scaffold that has been genetically engineered to organize various materials into nanowire (NW)-based mesoporous structures. In this study, high aspect-ratio titanium dioxide NWs are synthesized by utilizing M13 viruses as templates and the NWs are assembled into semiconducting mesoporous networks with tunable structural properties. To understand the effects of different morphologies on the photovoltaic performance, the as-fabricated networks are employed as photoanodes in liquid-state dye-sensitized solar cells (DSCs). Compared with traditional nanoparticle-based photoanodes, the NW-based DSC photoanodes demonstrate much higher electron diffusion lengths while maintaining a comparable light-harvesting capacity, thus leading to improved power conversion efficiencies. In addition, the NW-based semiconducting mesoporous thin films are able to load sufficient organolead iodide perovskite materials into the interconnected pores, and the perovskite-coated films are utilized as efficient photoanodes for solid-state organolead iodide perovskite hybrid solar cells (PSCs) and achieve better power conversion efficiencies compared to liquid-state DSCs.

KEYWORDS: M13 virus, titanium dioxide nanowires, three-dimensional mesoporous networks, dye-sensitized solar cells, organolead iodide perovskite hybrid solar cells

1. INTRODUCTION

Mesoporous semiconducting structures demonstrate advantages over bulk, macroporous materials and have been employed to improve the photo-electrochemical performance of catalytic electrodes, water splitting,¹ photonics,² and photovoltaics.^{3,4} Large active surface areas of mesoporous structure are beneficial to maximize catalytic or photoactive sites, loading of active materials, and amount of modified functional groups. Furthermore, continuous pathways within the semiconducting structures are critical to transport the photo-excited carriers to current collectors efficiently. To collect the carriers effectively, the recombination at the grain boundaries along percolative pathways must be minimized. Therefore, optimizing semiconducting architectures for practical photo-electrochemical applications requires a high degree of control over the spatial organization of nanomaterials within the mesoporous structures.

Bio-templated synthesis serves as an ideal synthetic approach, and the biological templates with desired morphology are utilized to direct the organization, nucleation, or growth of targeted materials into a functional matrix.^{5,6} The M13 virus, which is 880 nm in length and 6.6 nm in diameter, is a versatile biological scaffold that can be genetically engineered to organize nanomaterials into nanowire (NW)-based networks, including metals,⁷ perovskite materials,⁸ carbon materials,⁹ conducting polymers,¹⁰ and semiconductors. Titanium dioxide in the anatase nanocrystalline phase (n-TiO₂) is a widely-used wide bandgap semiconducting metal oxide for photo-electrochemical applications, such as water splitting, bulk-heterojunction solar cells, and sensitized solar cells.¹¹ Compared to traditional nanoparticle (NP)-based n-TiO₂ photoanodes, the NW-based n-TiO₂ photoanodes exhibit improved electron collection properties and also power

conversion efficiencies (PCEs).^{12, 13} Three-dimensional (3D) porous NW-based n-TiO₂ structures can be fabricated by utilizing M13 viruses as templates in various processes, including electrostatic self-assembly,¹³ hydrogel-templated method,¹² and covalent layer-by-layer assembly.¹⁴ Although each of these approaches yields a unique morphology and efficient photovoltaic performance, the fabrication processes can only achieve structures with a limited range of physical characteristics. For instance, covalent layer-by-layer assembly can make highly uniform nanoporous structures with thin NW diameters (<25 nm),¹⁴ whereas the hydrogel method produces hierarchical micro-porous films with large NW diameters (~200-300 nm).¹² In order to meet the myriad of functions required in photo-electrochemical applications, a more controllable synthetic technique is desired that enables the control of each morphological parameter – diameter of NWs, nano- and microporosity, and film thickness – independently during the fabrication process of mesoporous semiconducting networks.

In this study, a controllable fabrication process for mesoporous NW-based n-TiO₂ networks via M13 viruses as templates offers precise control over many of these features. Structural properties of the semiconducting networks can be engineered independently, including the extent of the conformal coating, diameter of NWs, size of crystallized particles, film thickness, and film porosity. First, the temperature of the hydrolysis reaction determines the extent of the conformal amorphous TiO₂ (a-TiO₂) nucleation to the virus surface. Likewise, by adjusting the concentration of TiO₂ precursor, the diameter of a-TiO₂ NWs can be precisely tuned. In the meantime, the size of crystallites comprising the annealed n-TiO₂ NWs strongly depends on the thickness of a-TiO₂ nucleated on the virus templates prior to annealing. Finally, the film porosity can be

tuned by adjusting the amount of sacrificial polymer blended with the a-TiO₂ NWs during film deposition. The effect of different morphologies on the photovoltaic performance of liquid-state dye-sensitized solar cells (DSCs) is investigated by employing the mesoporous semiconducting networks as the photoanodes. The optimized NW-based DSC photoanodes are compared with the NP-based DSC photoanodes and demonstrate much higher electron diffusion lengths (L_n), while maintaining similar light-harvesting capacities, leading to better PCEs. Furthermore, the NW-based semiconducting mesoporous networks exhibit high porosity and active surface area for the sufficient loading of perovskite materials; therefore, the perovskite-coated films can serve as efficient photoanodes for solid-state organolead iodide perovskite hybrid solar cells (PSCs). Moreover, these semiconducting 3D mesoporous networks demonstrate great potential for further applications in sensing, catalytic, and energy-storage electrodes.

2. EXPERIMENTAL METHODS

2.1. Materials. Titanium(IV) butoxide (Ti(OBu)₄), titanium (IV) chloride (TiCl₄), ethylene glycol, ethyl cellulose, terpineol, tert-butanol, 1-butyl-3-methylimidazolium iodide, iodine (I₂), guanidinium thiocyanate, 4-tert-butyl pyridine, valeronitrile, acetonitrile, isopropyl alcohol (IPA), and phosphate buffered saline (PBS) buffer solution were purchased from Sigma-Aldrich. Pure ethanol (200 Proof) was purchased from KOPTEC. Cis(diisothiocyanato)bis(2,2'-bipyridyl-4,4'-dicarboxylato)ruthenium(II) bis(tetrabutylammonium) (also named N719) and commercial TiO₂ NP paste (13/400 nm, Ti-Nanoxide D/SP) were purchased from Solaronix. N719 dye solution was prepared in acetonitrile and tert-butanol (volume ratio 1:1) mixture at 0.5 mM. The electrolyte

employed in DSCs was a solution of 0.6 M 1-butyl-3-methylimidazolium iodide, 0.03 M I₂, 0.10 M guanidinium thiocyanate, and 0.5 M 4-tert-butyl pyridine in a mixture of acetonitrile and valeronitrile (volume ratio 0.85:0.15).¹⁵ The E3M13 (AEEE expressed on the pVIII major coat protein) virus solution, $\sim 10^{14}$ virus mL⁻¹, was diluted to the desired concentration with PBS buffer. All water was deionized (18.2 M Ω , mill-Q pore). All reagents were used as received and without further purification.

2.2. Synthesis of amorphous TiO₂ (a-TiO₂) nanowires (NWs). The virus-templated a-TiO₂ NWs were synthesized by the following procedure. First, Ti(OBu)₄ was dissolved in pure ethanol (500 mL) at certain concentration (125 mg mL⁻¹, 250 mg mL⁻¹, and 500 mg mL⁻¹), and then the mixture was cooled down to the desired temperature. The temperature was controlled by using the mixture of ethylene glycol and ethanol with dry ice. To achieve the desired temperature, solutions of ethylene glycol and ethanol in various volume ratios were mixed, and then enough dry ice chunks were placed into the cooling solution. After the temperature was stabilized for 15 minutes, the solution of $\sim 1.63 \times 10^{14}$ virus in 25 ml PBS buffer was poured into the cold Ti(OBu)₄/ethanol mixtures while stirring vigorously. The solution was stirred overnight to complete the reaction. After the overnight reaction, the products of virus-templated TiO₂ NWs were centrifuged at 3000 r.p.m. for 30 minutes. The products were rinsed multiple times with pure ethanol. The as-synthesized a-TiO₂ NWs were observed via JEOL 200CX transmission electron microscopy (TEM) with an accelerating voltage of 120 kV, JEOL 2010 HRTEM with an accelerating voltage of 200 kV.

2.3. Fabrication of the NW-based anatase TiO₂ (n-TiO₂) photoanodes. After the excess ethanol was removed, the products were blended with terpineol and sacrificial polymers

(*e.g.*, ethyl cellulose). The weight of sacrificial polymers is controlled at 50 wt.%, 100 wt.% and 200 wt.% of the synthesized TiO₂ products to achieve different film porosities. Afterwards, the ethanol was removed by rotary-evaporation, and the viscous pastes for doctor-blading and spin-coating were formed. The FTO substrates for DSCs were cleaned by sonication in an aqueous soap solution, milli-Q water, acetone, and IPA sequentially. The clean substrates were subjected to an ultraviolet/ozone treatment for 30 minutes and then immersed in a 40 mM aqueous TiCl₄ solution at 80 °C for 30 minutes and washed with water and ethanol. By using spin-coating and doctor-blading, the commercial NP-based paste and the virus-templated NW-based paste are both coated on the FTO substrates. The NP-based and virus-templated NW-based TiO₂ films in desired thickness were achieved by either doctor-blading or spin-coating on FTO substrates. After drying at 100 °C, the TiO₂ films were gradually heated to 500 °C for 30 minutes. The processes (doctor-blading/spin-coating and annealing) were repeated several times to achieve the optimal thickness of DSC photoanodes (over 10 μm). Film thickness was monitored using a surface profilometer (Veeco Dektak). Scanning electron microscopy (SEM) images of the film morphology were obtained using Helios Nanolab 600 Dual Beam Focused Ion Beam System. X-ray diffraction (XRD) patterns were collected (PANalytical Multipurpose Diffractometer, Cu Kα radiation operated at 40 kV and 40 mA) using a step size of 0.02° with 6.0° per minute scan speeds under the following settings: 2° of anti-scatter slit, 6 mm of irradiated length of automatic mode and 0.04 rad of soller slit.

2.4. Fabrication of dye-sensitized solar cells (DSCs). After calcination, the DSC photoanodes were cooled to 80 °C and immersed in the N719 solution, and kept at room

temperature over 24 hours. The counter-electrode was a 100-nm-thick platinum film sputtered on a FTO substrate. The dyed TiO₂ photoanodes and platinum counter-electrodes were assembled into a sandwich-type cell with the liquid electrolyte and sealed with a hot-melt 25 μm Surlyn (Solaronix). The final photoanode had dimensions of ~0.16 cm² (4 mm × 4 mm), further determined from a calibrated digital camera image. The dye loading of the photoanode was determined by eluting the N719 dye from the TiO₂ electrode into a known amount of 0.3 M NaOH and using a UV-Vis calibration curve to determine the concentration of dye in solution to total amount of dye per film volume.

2.5. Fabrication of organolead iodide perovskite hybrid solar cells (PSCs). The ~500-nm-thick NW-based PSC photoanodes were fabricated by spin-coating the paste at 3000 r.p.m. for 30 seconds. After drying at 100 °C, the TiO₂ films were gradually heated to 500 °C for 30 minutes. Lead iodide (PbI₂) was dissolved in dimethylformamide at a concentration of 462 mg mL⁻¹ (~1 M) under stirring at 80 °C. The solution was kept at 80 °C during the whole procedure. The photoanodes were then infiltrated with PbI₂ by spin-coating the solution at 5000 r.p.m. for 30 seconds and dried at 80 °C for 30 minutes. After cooling to room temperature, the films were dipped in a solution of CH₃NH₃I in IPA (10 mg mL⁻¹) for 1 minute, rinsed with IPA for 1 minute and dried at 80 °C for 30 minutes. The hole-transporting material was then deposited by spin-coating at 4000 r.p.m. for 30 seconds. The spin-coating solution was prepared by dissolving 72.3 mg (spiro-MeOTAD), 28.8 μL 4-tert-butylpyridine, 17.5 μL of a stock solution of 520 mg mL⁻¹ lithium bis(trifluoromethylsulphonyl) imide in acetonitrile in 1 mL chlorobenzene. Finally, 80 nm of gold was thermally evaporated on top of the device.

2.6. *Characterization of solar cells.* Photovoltaic measurements were performed using an AM 1.5 solar simulator (Photo Emission Tech.). The power of the simulated light was calibrated to 100 mW cm^{-2} by using a reference silicon photodiode with a power meter (1835-C, Newport) and a reference silicon solar cell to reduce the mismatch between the simulated light and AM 1.5. J-V curves were obtained by applying an external bias to the cell and measuring the generated photocurrent with a Keithley model 2400 digital source meter. The voltage step and delay time of photocurrent were 10 mV and 40 ms, respectively. Electrochemical impedance spectroscopy (EIS) of solar cells was measured using a Solartron 1260 frequency response analyzer. The photoanodes of both DSC and PSC were connected to the working electrodes. The counter electrodes were connected to the auxiliary electrodes and reference electrodes. The impedance measurements of both DSC and PSC were carried out at forward bias in dark conditions. The spectra were measured at various forward bias voltages in the frequency range $\sim 0.1 \text{ Hz}$ to $\sim 1 \text{ MHz}$ with oscillation potential amplitudes of 10 mV at room temperature. The applied forward bias voltage was changed by 50 mV steps from 1000 mV to 0 mV. The impedance measurements were carried out at forward bias in dark conditions. The obtained impedance spectra were fit to the reported model of DSCs¹⁶ and PSCs¹⁷⁻²¹ with Z-view software (v3.2b, Scribner Associates).

3. RESULTS AND DISCUSSION

Figure 1A illustrates the process developed to construct mesoporous semiconducting networks utilizing M13 viruses as templates. First, the TiO_2 precursor (*i.e.*, $\text{Ti}(\text{OBU})_4$) is dissolved in ethanol at low temperature ($< -40 \text{ }^\circ\text{C}$), and an aqueous virus

solution is then added into the solution at constant temperature. Then, as the solution is allowed to warm back to room temperature, the virus-templated a-TiO₂ NWs are precipitated, centrifuged, and washed. After the purified products are collected, the a-TiO₂ NWs are blended with sacrificial polymers in terpineol to prevent the annealed film from cracking and to control the film porosity. Either a spin-coating or doctor-blading method is used to deposit the film and control its thickness. The amorphous coated films are then annealed at 500 °C in order to (1) remove the virus templates and polymers through high temperature oxidation, (2) convert the a-TiO₂ into nanocrystalline n-TiO₂, and (3) sinter neighboring nanocrystals as well as nanowires together to form an interconnected, percolative network. By controlling the fabrication parameters at each step, a wide range of film morphologies can be achieved.

Controlling the rate of hydrolysis of Ti(OBu)₄ is critical for tuning the extent of conformal nucleation of a-TiO₂ along the M13 virus. Although transition metal alkoxides hydrolyze rapidly with water, the rate can be depressed by performing the reaction at lower temperatures.²² The influence of reaction temperature on the morphologies of a-TiO₂ NWs coated on M13 viruses is observed by TEM, and the results are shown in **Figure 1B-1E**. The a-TiO₂ products synthesized at room temperature (Figure 1B) and 0 °C (Figure 1C) are thick, highly bridged and heavily aggregated due to the rapid hydrolysis reaction. As the reaction temperature decreases to -20 °C (Figure 1D) or further to -40 °C (Figure 1E), the reaction rate is reduced and nearly terminated. As the cold solutions slowly return to room temperature naturally, the hydrolysis of Ti(OBu)₄ (**Equation 1**) and the following condensation of a-TiO₂ (**Equation 2**) take place gradually on the hydrophilic viral surfaces, resulting in a conformal coating of a-TiO₂.



Since almost all of the nucleation occurs at the virus surface, conformally coated a-TiO₂ NWs with diameters of 20 nm (20-nm-NWs, **Figure 2A**), 30 nm (30-nm-NWs, **Figure 2B**), and 40 nm (40-nm-NWs, **Figure 2C**) can be achieved by adjusting the concentration of Ti(OBu)₄ to 125 mg mL⁻¹, 250 mg mL⁻¹, and 500 mg mL⁻¹ in cold water/ethanol solution, respectively. Controlled by the length of the virus template, the length of synthesized NWs is always fixed at 1 μm, yielding the NWs with high aspect ratios between 25 and 40. **Figure 2D** shows a TEM image of an annealed n-TiO₂ NW with a 7-nm diameter virus-shaped cavity in the interior, which clearly demonstrates that the NWs utilize the viruses as templates for deposition. The annealing process removes the virus templates and crystallizes a-TiO₂ NWs into n-TiO₂, confirmed by XRD analysis (**Figure 2E**). The lattice of n-TiO₂ with a spacing of ~3.6 Å is directly observed by TEM (Figure 2E inset). The annealed 20-nm-NWs exhibit a wider n-TiO₂ peak at ~26 degree, compared to the width of the annealed 30-nm-NWs and 40-nm-NWs. The larger peak width indicates that the size of n-TiO₂ nanocrystallites along the annealed 20-nm-NW is smaller than those formed on 30- and 40-nm-NWs.^{23, 24}

In order to visualize the nanocrystallites forming the NWs, the annealed n-TiO₂ NWs are disintegrated by ultrasonication, and the disassembled crystallites are characterized by TEM in **Figure 3A-3C**. In Figure 3A, the size of crystallites forming annealed 20-nm-NWs is smaller than 10 nm, resulting from the thin constrained region of nucleation of a-TiO₂ on the virus templates. Such small crystallites result in more grain boundaries along any given conductive pathways, which lead to an increased electron

diffusion resistance and increased recombination opportunities of photo-excited carriers at the NW surface. On the other hand, 30-nm-NWs and 40-nm-NWs exhibit thicker coatings, which form nanocrystals larger than 15 nm (Figure 3B, 3C) upon annealing, which agrees with the reported optimal particle size to achieve efficient electron collection within the DSC photoanodes.^{3, 23-25}

The porosity of NW-based films can be controlled by blending a sacrificial polymer (*i.e.*, ethylene cellulose) with a-TiO₂ NWs prior to film deposition by doctor-blading or spin-coating. The ethylene cellulose serves several purposes: (1) after a-TiO₂ NWs are blended with the polymer, viscous pastes are formed and able to ease the deposition of uniform films; (2) the polymer concentration in the paste determines the final film porosity because the polymer is removed during the annealing process, leaving behind voids in the n-TiO₂ NW-based network; and (3) it helps prevent the formation of large cracks during the annealing process (**Figure S1**). The final mesoporous networks are composed of tightly packed n-TiO₂ crystallites forming interconnected porous NWs, which persist throughout the entire film and provide directional pathways for improved carrier transport (**Figure 3D**). Such a permeable matrix with interconnected pores maximizes interfacial contact with the electrolyte, thereby increasing the mobility of redox couples and minimizing back-recombination. Additionally, the existence of pores smaller than 20 nm is observed by high-resolution SEM (**Figure 3E**), which confirms that a large active surface area per film volume is available for promoting photo-electrochemical reactions. Blending the 20-nm-NWs, 30-nm-NWs, or 40-nm-NWs with different amounts of sacrificial polymer systematically modulates the morphology and porosity of mesoporous semiconducting networks (SEM images in **Figure 4A-4I**).

It is expected from previous reports that optimal photovoltaic performance of sensitized solar cells would be achieved by photoanodes exhibiting film porosities around 50%.^{26, 27} The mesoporous semiconducting networks constructed by n-TiO₂ 20-nm-NWs (20-nm-NW thin film, **Figure 4A**), n-TiO₂ 30-nm-NWs (30-nm-NW thin film, **Figure 4B**), and n-TiO₂ 40-nm-NWs (40-nm-NW thin film, **Figure 4C**) can be tuned to achieve the film porosities around 52.3%, 51.6% and 51.9%, respectively, as determined by analyzing SEM images with the program *ImageJ*. The pore size distribution calculated from Figure 4A-4C is shown in **Figure 5A-5C**. The average pore diameter of the films increases with increasing NW diameter; equivalent pore diameters sized 16.6 nm, 18.3 nm, and 21.2 nm are achieved using n-TiO₂ 20-, 30-, and 40-nm-NWs as building-block-units of mesoporous thin films, respectively.

To investigate and quantify the effect of different morphologies on the photo-electrochemical mechanisms, the semiconducting mesoporous thin films are employed as photoanodes and assembled into DSCs. The PCEs of virus-templated DSCs are optimized by varying the thickness of the photoanodes (**Figure S2**), and the optimal thickness of DSC photoanodes is about 12-14 μm . Since the charge separation efficiency approaches unity when the N719 dye and n-TiO₂ are used, the overall device performance is governed by the ability of the photoanodes to harvest light and transport photo-generated electrons. First, the light-harvesting capability of a DSC photoanode is proportional to the amount of dye that is adsorbed onto the photoanode, which highly depends on the available active surface area of the n-TiO₂ mesoporous structures. The n-TiO₂ thin films are soaked in the dye solution, and the dye loading is quantified by desorbing the dye molecules from the n-TiO₂ surface. By analyzing the absorption of the dye solution, the

dye loading (**Figure 6A**) of the NW-based thin films are calculated and compared with the photoanodes made by commercial TiO₂ NP paste. In Figure 6A, the 20-nm-NW photoanode shows a similar amount of dye loading (96.7 mmole cm⁻³) as the NP-based photoanode (101.4 mmole cm⁻³), indicating similar light-harvesting capability of the photoanodes. As the NW diameter increases to 30 nm and 40 nm, the dye loading of the photoanodes slightly decreases to 85.3 mmole cm⁻³ and 74.6 mmole cm⁻³, respectively. The decreased dye loading results from the lower surface-to-volume ratio of the NWs and larger average pores in the thin films, thus the reduced active surface area.

In addition, to understand the electron-transporting properties of the photoanodes constructed by different NW-based morphologies, the EIS are measured after the DSCs are assembled. The L_n of DSC photoanodes shown in **Figure 6B** is calculated from the Nyquist diagrams. The detailed Nyquist diagram at higher frequency and the fitting results at 725 mV are also shown in **Figure S3**. These results along with the corresponding efficiencies of electron collection (η_{COL}) are summarized in **Table 1**. The details of the calculations for determining L_n and η_{COL} are provided in Supporting Information.^{16, 28, 29} As shown in Figure 6B and Table 1, the 30-nm-NW and 40-nm-NW photoanodes exhibit longer L_n (93.9 μm and 76.1 μm) and higher η_{COL} (99.5% and 99.3%) than the n-TiO₂ NP-based photoanodes (37.1 μm , 93.9%), respectively. The 3D network composed of interconnected n-TiO₂ NWs improves electron-transporting property by reducing opportunities for interfacial recombination and thus lengthening electron lifetimes. However, the 20-nm-NW photoanode exhibits a shorter L_n (6.8 μm) and an inefficient η_{COL} (51.2%). This is believed to be due to the small size of the

nanocrystallites (<10 nm) in the photoanodes, which leads to increased photo-carrier recombination at numerous grain boundaries along the n-TiO₂ NWs.

After the light-harvesting and electron-transporting properties of the photoanodes are both characterized, the overall photo-electrochemical performance of DSCs employing the mesoporous n-TiO₂ NW-based photoanodes are measured and compared to the DSCs with n-TiO₂ NP-based photoanodes. The average and highest PCE among ~5-10 DSCs for each kind of photoanode are shown in **Figure 6C**. The current density-voltage (*J-V*) curves of the most efficient DSCs are plotted in **Figure 6D**. The related photovoltaic parameters, including open circuit voltage (V_{OC}), fill factor (FF), short-circuit current density (J_{SC}), PCE, L_n , η_{COL} , and dye loading, are summarized in Table 1. In order to achieve efficient device performance, the light-harvesting capability and electron-transporting property of the mesoporous structures are required to be optimized simultaneously. Otherwise, insufficient photo-excited electrons are generated or the electrons are easily lost due to radiative recombination during electron collection. For instance, the 40-nm-NW DSC shows improved electron-transport properties over the NP-based DSCs, but insufficient dye loading results in a lower light-harvesting capability and thus reduced overall photovoltaic performance. On the other hand, even though the 20-nm-NW DSC exhibits a similar light-harvesting capability as the NP-based DSC, the device performance is much lower than the NP-based DSC due to the lower L_n . By optimizing both the active surface area and the size of crystallites in the mesoporous structures, the 30-nm-NW DSC demonstrates balanced light-harvesting and electron-transporting abilities, exhibiting a higher PCE (7.1%) and J_{SC} (14.0 mA cm⁻²) than the NP-based DSC (6.6% and 12.3 mA cm⁻²). Despite having a slightly lower light-

harvesting capability, the 30-nm-NW photoanodes composed of interconnected NWs provide more efficient electron diffusion pathways to transport photo-excited electrons to the current collector, leading to increased charge collection efficiencies and improved PCEs over the NP-based DSCs.

In addition, the NW-based semiconducting mesoporous thin films are utilized as the photoanodes of solid-state PSCs. Since organolead iodide perovskite materials are known as efficient light-harvesters and electron-transporters, the architecture of solid-state PSCs is quite different from that of liquid-state DSCs.³⁰⁻³⁴ For instance, the optimal thickness of n-TiO₂ PSC photoanodes (~0.5 μm) is much thinner than that of DSC photoanodes (>10 μm). To achieve this thickness, the thin films are fabricated via spin-coating process followed by high-temperature annealing. After the PSCs are assembled by employing 30-nm-NW thin films, they are characterized by EIS under dark conditions to understand the resistance to charge recombination (**Figure 7A**). Nyquist diagrams of solid-state PSCs employing 30-nm-NW photoanodes at 700 mV are shown in **Figure S4A-S4C**. Nyquist diagrams at 700 mV (**Figure S4A**) are both enlarged to observe the detailed features in the intermediate (**Figure S4B**) and high frequency regions (**Figure S4C**). After the NW-based PSC is characterized by EIS, the spectra are analyzed using a reported model.¹⁷⁻²¹ The recombination resistances of the PSCs employing 30-nm-NW photoanode shown in **Figure 7A** are similar to the results reported in the literature.¹⁸ Also, **Figure 7B** shows a histogram of the PCEs from batches of ~25 PSCs employing 30-nm-NW photoanodes. Histogram plots of solar cell performance parameters, including V_{OC} , J_{SC} , and FF are also shown in **Figure S5A-S5C**, respectively. The inset of **Figure 7C** presents the average PCE and the highest PCE from batches of PSCs. The highest PCE is

7.5% with a high J_{SC} around 17.8 mA cm^{-2} . The distributions of photovoltaic performances of the PSCs are disperse, which is also observed in the literature.^{21, 31} The J - V curve of the most efficient PSC is plotted in **Figure 7C**, and the related photovoltaic parameters are listed in Table 1. From the EIS and photovoltaic measurements, it is clearly demonstrated that the mesoporous NW-based n-TiO₂ structures with high porosity and interconnected pores allow high loading of organolead iodide perovskite materials. The organolead iodide perovskite-coated NW-based n-TiO₂ structures can be served as efficient photoanodes with sufficient light-absorption and high electron-transporting properties, leading to better PCEs than the liquid-state DSCs. With on-going optimization on the fabrication process of PSCs, the photovoltaic performance can be further improved.

CONCLUSION

In summary, we report an improved approach to synthesizing a-TiO₂ NWs via using M13 viruses as templates and assembling the NWs into mesoporous semiconducting networks. This tunable fabrication process provides the opportunities to tune important structural parameters independently, including the extent of conformal coating, diameter of NWs, size of crystallites, film thickness, and film porosity. To understand the effects of different morphologies on the photovoltaic performance of DSCs and PSCs, the mesoporous semiconducting networks are utilized as the photoanodes in both DSCs and PSCs. Compared with the NP-based DSC photoanodes, the NW-based DSC photoanodes demonstrate much higher L_n and similar light-harvesting capacities, leading to better PCEs. Also, the mesoporous NW-based n-TiO₂

structures enable the high loading of organolead iodide perovskite materials in the interconnected pores. The perovskite-coated structures can be utilized as efficient photoanodes and lead to better PCEs than the liquid-state DSCs. Moreover, the mesoporous semiconducting networks are expected to be useful in other energy related applications due to their versatility, ability to rapidly transport electrons, and potential to organize different functional materials via protein recognition. **Figure S6A-S6E** shows an example of synthesizing core-shell structures of gold nanoparticles (AuNPs) and TiO₂ NWs by binding the AuNPs on M13 virus prior to the a-TiO₂ nucleation (Figure S6A and S6B). After the annealing, the AuNPs@n-TiO₂ NWs structure can be synthesized (Figure S6D and S6E), and confirmed by XRD analysis (Figure S6C). Specifically, the morphology of the networks can be controlled to meet the structural requirements needed for optimization of highly porous NW electrodes for the active phase of supercapacitors, lithium ion batteries and water splitting devices.

AUTHOR CONTRIBUTIONS

P.-Y.C., X.D., A.M.B. and P.T.H. conceived the idea and designed the experiments. P.-Y.C. performed the synthesis and SEM imaging. P.-Y.C. and X.D. performed the TEM imaging. P.-Y.C., X.D. and M.T.K. performed the fabrication and characterization of the solar cells. J.Q. performed the XRD measurement. N.-M.D.C. performed the XPS measurement. P.-Y.C., X.D., M.T.K., P.T.H. and A.M.B. co-wrote the paper and all authors discussed the results and commented on the manuscript.

FUNDING SOURCES

This work was supported by Eni, S.p.A (Italy) through the MIT Energy Initiative Program. P.-Y.C., M.T.K. and N.-M.D.C. acknowledge support from the MIT Energy Initiative Eni-MIT Energy Fellowship. N.-M.D.C. also acknowledges the Postgraduate Scholarship support from the Natural Sciences and Engineering Research Council of Canada (NSERC).

SUPPORTING INFORMATION

Microscopy images of the annealed NW-based n-TiO₂ films without and with employing the sacrificial polymers, dependence of PCE on the thickness of DSC photoanode, Nyquist diagrams of the EIS obtained under dark condition for different kinds of DSCs at 725 mV, calculation of L_n and η_{COL} , Nyquist diagrams of the EIS obtained under dark condition for PSCs employing the 30-nm-NW photoanodes, static data of photovoltaic performance of PSCs employing the 30-nm-NW n-TiO₂ photoanodes, and characterizations (TEM, XRD analysis) of AuNP@TiO₂ core-shell nanostructures are provided in the Supporting Information. This material is available free of charge *via* the Internet at <http://pubs.acs.org>.

ACKNOWLEDGEMENT

The authors wish to dedicate this paper to the memory of Officer Sean Collier, for his caring service to the MIT community and for his sacrifice.

REFERENCES

- (1) Hartmann, P.; Lee, D.-K.; Smarsly, B. M.; Janek, J., Mesoporous TiO₂: Comparison of Classical Sol-Gel and Nanoparticle Based Photoelectrodes for the Water Splitting Reaction. *ACS Nano* **2010**, *4* (6), 3147-3154.
- (2) Innocenzi, P.; Malfatti, L., Mesoporous Thin Films: Properties and Applications. *Chem. Soc. Rev.* **2013**, *42* (9), 4198-4216.
- (3) Hagfeldt, A.; Boschloo, G.; Sun, L.; Kloo, L.; Pettersson, H., Dye-Sensitized Solar Cells. *Chem. Rev.* **2010**, *110* (11), 6595-6663.
- (4) Kamat, P. V.; Tvrdy, K.; Baker, D. R.; Radich, J. G., Beyond Photovoltaics: Semiconductor Nanoarchitectures for Liquid-Junction Solar Cells. *Chem. Rev.* **2010**, *110* (11), 6664-6688.
- (5) Jorgensen, M. R.; Bartl, M. H., Biotemplating Routes to Three-Dimensional Photonic Crystals. *J. Mater. Chem.* **2011**, *21* (29), 10583-10591.
- (6) Li, F.; Wang, Q., Fabrication of Nanoarchitectures Templated by Virus-Based Nanoparticles: Strategies and Applications. *Small* **2014**, *10* (2), 230-245.
- (7) Sawada, T.; Kang, S.; Watanabe, J.; Mihara, H.; Serizawa, T., Hybrid Hydrogels Composed of Regularly Assembled Filamentous Viruses and Gold Nanoparticles. *ACS Macro Lett.* **2014**, *3* (4), 341-345.
- (8) Cung, K.; Han, B. J.; Nguyen, T. D.; Mao, S.; Yeh, Y.-W.; Xu, S.; Naik, R. R.; Poirier, G.; Yao, N.; Purohit, P. K.; McAlpine, M. C., Biotemplated Synthesis of PZT Nanowires. *Nano Lett.* **2013**, *13* (12), 6197-6202.
- (9) Dang, X.; Yi, H.; Ham, M.-H.; Qi, J.; Yun, D. S.; Ladewski, R.; Strano, M. S.; Hammond, P. T.; Belcher, A. M., Virus-Templated Self-Assembled Single-Walled Carbon Nanotubes for Highly Efficient Electron Collection in Photovoltaic Devices. *Nat. Nano* **2011**, *6* (6), 377-384.
- (10) Chen, P.-Y.; Hyder, M. N.; Mackanic, D.; Courchesne, N.-M. D.; Qi, J.; Klug, M. T.; Belcher, A. M.; Hammond, P. T., Assembly of viral hydrogels for three-dimensional conducting nanocomposites. *Adv. Mater.* **2014**, In Press.
- (11) Chen, X.; Mao, S. S., Titanium Dioxide Nanomaterials: Synthesis, Properties, Modifications, and Applications. *Chem. Rev.* **2007**, *107* (7), 2891-2959.
- (12) Chen, P.-Y.; Dang, X.; Klug, M. T.; Qi, J.; Dorval Courchesne, N.-M.; Burpo, F. J.; Fang, N.; Hammond, P. T.; Belcher, A. M., Versatile Three-Dimensional Virus-Based Template for Dye-Sensitized Solar Cells with Improved Electron Transport and Light Harvesting. *ACS Nano* **2013**, *7* (8), 6563-6574.
- (13) Chen, P.-Y.; Ladewski, R.; Miller, R.; Dang, X.; Qi, J.; Liau, F.; Belcher, A. M.; Hammond, P. T., Layer-by-Layer Assembled Porous Photoanodes for Efficient Electron Collection in Dye-Sensitized Solar Cells. *J. Mater. Chem. A* **2013**, *1* (6), 2217-2224.
- (14) Courchesne, N.-M. D.; Klug, M. T.; Chen, P.-Y.; Kooi, S. E.; Yun, D. S.; Hong, N.; Fang, N. X.; Belcher, A. M.; Hammond, P. T., Assembly of a Bacteriophage-Based Template for the Organization of Materials into Nanoporous Networks. *Adv. Mater.* **2014**, *26* (21), 3398-3404.
- (15) Ito, S.; Murakami, T. N.; Comte, P.; Liska, P.; Grätzel, C.; Nazeeruddin, M. K.; Grätzel, M., Fabrication of Thin Film Dye Sensitized Solar Cells with Solar to Electric Power Conversion Efficiency over 10%. *Thin Solid Films* **2008**, *516* (14), 4613-4619.
- (16) Halme, J.; Vahermaa, P.; Miettunen, K.; Lund, P., Device Physics of Dye Solar Cells. *Adv. Mater.* **2010**, *22* (35), E210-E234.

- (17) Bisquert, J., Theory of the Impedance of Electron Diffusion and Recombination in a Thin Layer. *J. Phys. Chem. B* **2001**, *106* (2), 325-333.
- (18) Dualeh, A.; Moehl, T.; Tétreault, N.; Teuscher, J.; Gao, P.; Nazeeruddin, M. K.; Grätzel, M., Impedance Spectroscopic Analysis of Lead Iodide Perovskite-Sensitized Solid-State Solar Cells. *ACS Nano* **2014**, *8* (1), 362-373.
- (19) Fabregat-Santiago, F.; Bisquert, J.; Cevey, L.; Chen, P.; Wang, M.; Zakeeruddin, S. M.; Grätzel, M., Electron Transport and Recombination in Solid-State Dye Solar Cell with Spiro-OMeTAD as Hole Conductor. *J. Am. Chem. Soc.* **2008**, *131* (2), 558-562.
- (20) Gonzalez-Pedro, V.; Juarez-Perez, E. J.; Arsyad, W.-S.; Barea, E. M.; Fabregat-Santiago, F.; Mora-Sero, I.; Bisquert, J., General Working Principles of $\text{CH}_3\text{NH}_3\text{PbX}_3$ Perovskite Solar Cells. *Nano Lett.* **2014**, *14* (2), 888-893.
- (21) Kim, H.-S.; Mora-Sero, I.; Gonzalez-Pedro, V.; Fabregat-Santiago, F.; Juarez-Perez, E. J.; Park, N.-G.; Bisquert, J., Mechanism of Carrier Accumulation in Perovskite Thin-Absorber Solar Cells. *Nat. Commun.* **2013**, *4*.
- (22) Yoldas, B., Hydrolysis of Titanium Alkoxide and Effects of Hydrolytic Polycondensation Parameters. *J. Mater. Sci.* **1986**, *21* (3), 1087-1092.
- (23) Chou, T. P.; Zhang, Q.; Russo, B.; Fryxell, G. E.; Cao, G., Titania Particle Size Effect on the Overall Performance of Dye-Sensitized Solar Cells. *J. Phys. Chem. C* **2007**, *111* (17), 6296-6302.
- (24) Nakade, S.; Saito, Y.; Kubo, W.; Kitamura, T.; Wada, Y.; Yanagida, S., Influence of TiO_2 Nanoparticle Size on Electron Diffusion and Recombination in Dye-sensitized TiO_2 Solar Cells. *J. Phys. Chem. B* **2003**, *107* (33), 8607-8611.
- (25) Hosni, M.; Kusumawati, Y.; Farhat, S.; Jouini, N.; Pauporté, T., Effects of Oxide Nanoparticle Size and Shape on Electronic Structure, Charge Transport, and Recombination in Dye-Sensitized Solar Cell Photoelectrodes. *J. Phys. Chem. C* **2014**.
- (26) Ni, M.; Leung, M. K. H.; Leung, D. Y. C.; Sumathy, K., An Analytical Study of the Porosity Effect on Dye-Sensitized Solar Cell Performance. *Sol. Energ. Mat. Sol.* **2006**, *90* (9), 1331-1344.
- (27) van de Lagemaat, J.; Benkstein, K. D.; Frank, A. J., Relation Between Particle Coordination Number and Porosity in Nanoparticle Films: Implications to Dye-Sensitized Solar Cells. *J. Phys. Chem. B* **2001**, *105* (50), 12433-12436.
- (28) Bisquert, J.; Fabregat-Santiago, F.; Mora-Seró, I.; Garcia-Belmonte, G.; Giménez, S., Electron Lifetime in Dye-Sensitized Solar Cells: Theory and Interpretation of Measurements. *J. Phys. Chem. C* **2009**, *113* (40), 17278-17290.
- (29) Wang, M.; Chen, P.; Humphry-Baker, R.; Zakeeruddin, S. M.; Grätzel, M., The Influence of Charge Transport and Recombination on the Performance of Dye-Sensitized Solar Cells. *ChemPhysChem* **2009**, *10* (1), 290-299.
- (30) Burschka, J.; Pellet, N.; Moon, S.-J.; Humphry-Baker, R.; Gao, P.; Nazeeruddin, M. K.; Grätzel, M., Sequential Deposition as a Route to High-Performance Perovskite-Sensitized Solar Cells. *Nature* **2013**, *499* (7458), 316-319.
- (31) Lee, M. M.; Teuscher, J.; Miyasaka, T.; Murakami, T. N.; Snaith, H. J., Efficient Hybrid Solar Cells Based on Meso-Superstructured Organometal Halide Perovskites. *Science* **2012**, *338* (6107), 643-647.
- (32) Liu, M.; Johnston, M. B.; Snaith, H. J., Efficient Planar Heterojunction Perovskite Solar Cells by Vapour Deposition. *Nature* **2013**, *501* (7467), 395-398.

- (33) Stranks, S. D.; Eperon, G. E.; Grancini, G.; Menelaou, C.; Alcocer, M. J. P.; Leijtens, T.; Herz, L. M.; Petrozza, A.; Snaith, H. J., Electron-Hole Diffusion Lengths Exceeding 1 Micrometer in an Organometal Trihalide Perovskite Absorber. *Science* **2013**, *342* (6156), 341-344.
- (34) Xing, G.; Mathews, N.; Sun, S.; Lim, S. S.; Lam, Y. M.; Grätzel, M.; Mhaisalkar, S.; Sum, T. C., Long-Range Balanced Electron- and Hole-Transport Lengths in Organic-Inorganic $\text{CH}_3\text{NH}_3\text{PbI}_3$. *Science* **2013**, *342* (6156), 344-347.

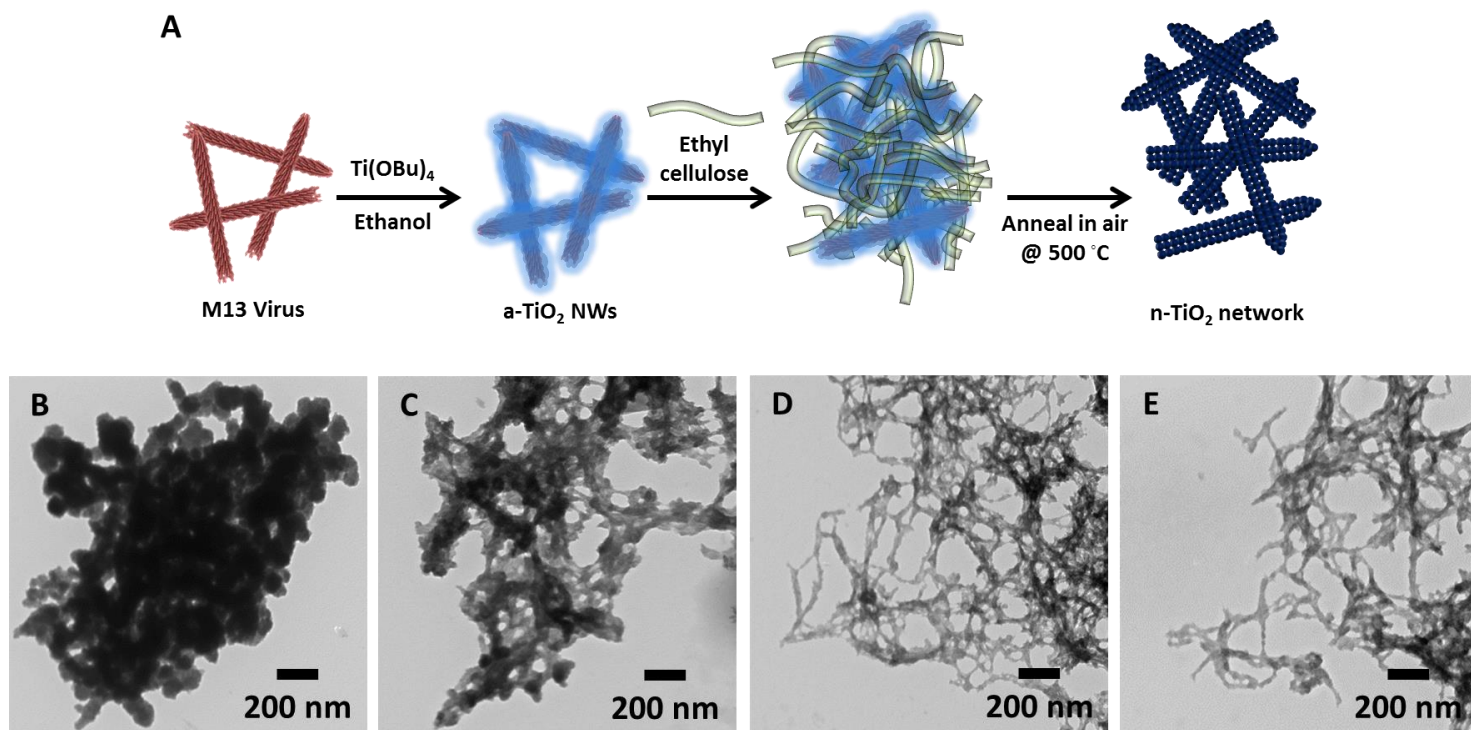


Figure 1. A. Schematic illustration of the controllable fabrication process of n-TiO₂ NW-based networks via utilizing M13 viruses as templates. The as-fabricated NW-based n-TiO₂ networks are employed as the photoanodes for DSCs and PSCs to understand the effect of different morphologies on the photovoltaic performance. TEM images of the a-TiO₂ NWs synthesized at different hydrolysis temperatures at B. 20 °C, C. 0 °C, D. -20 °C, and E. -40 °C.

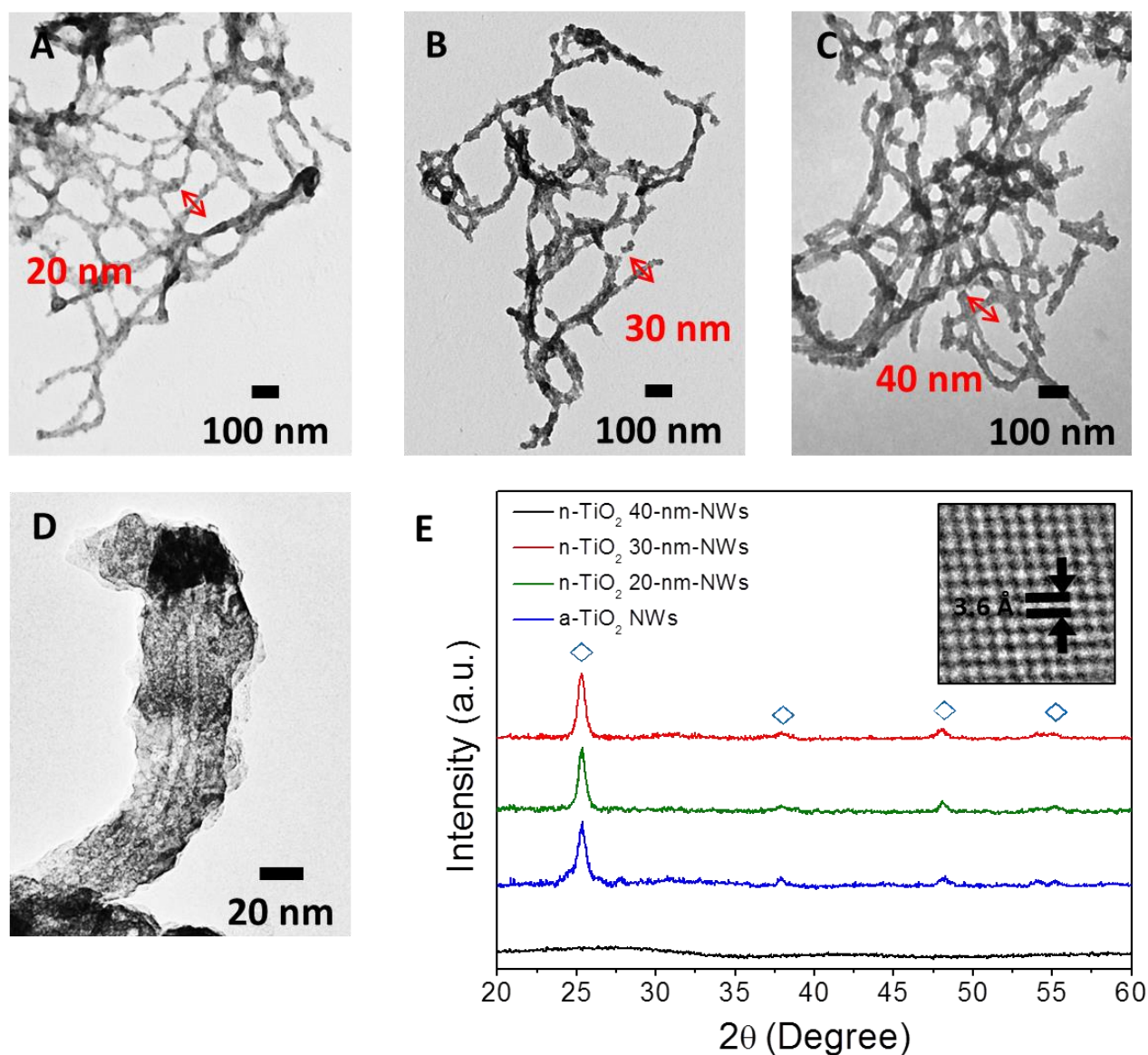


Figure 2. TEM images of the a-TiO₂ NWs using M13 viruses as templates. The uniformly-coated a-TiO₂ NWs with diameters around 20 nm (20-nm-NWs), 30 nm (30-nm-NWs), and 40 nm (40-nm-NWs) are shown in Figure 2A, 2B, and 2C, respectively. The TEM images demonstrate that the diameter of NWs can be precisely controlled by the concentration of Ti(OBu)₄ in the low-temperature hydrolysis reaction. D. TEM image of the annealed NW with a cavity (diameter ~7 nm) in the center, indicating that the viral templates are burned off during the high-temperature annealing. E. XRD analysis of the a-TiO₂ NWs after the low-temperature hydrolysis and the n-TiO₂ NWs after the high-temperature annealing. The blue diamond symbols indicate the peaks of n-TiO₂ phase, and TEM image of the n-TiO₂ nanocrystallites with lattice constant ~3.6 Å is shown in the inset of Figure 1E. The XRD analysis demonstrates that the a-TiO₂ products crystallize into the n-TiO₂ structures.

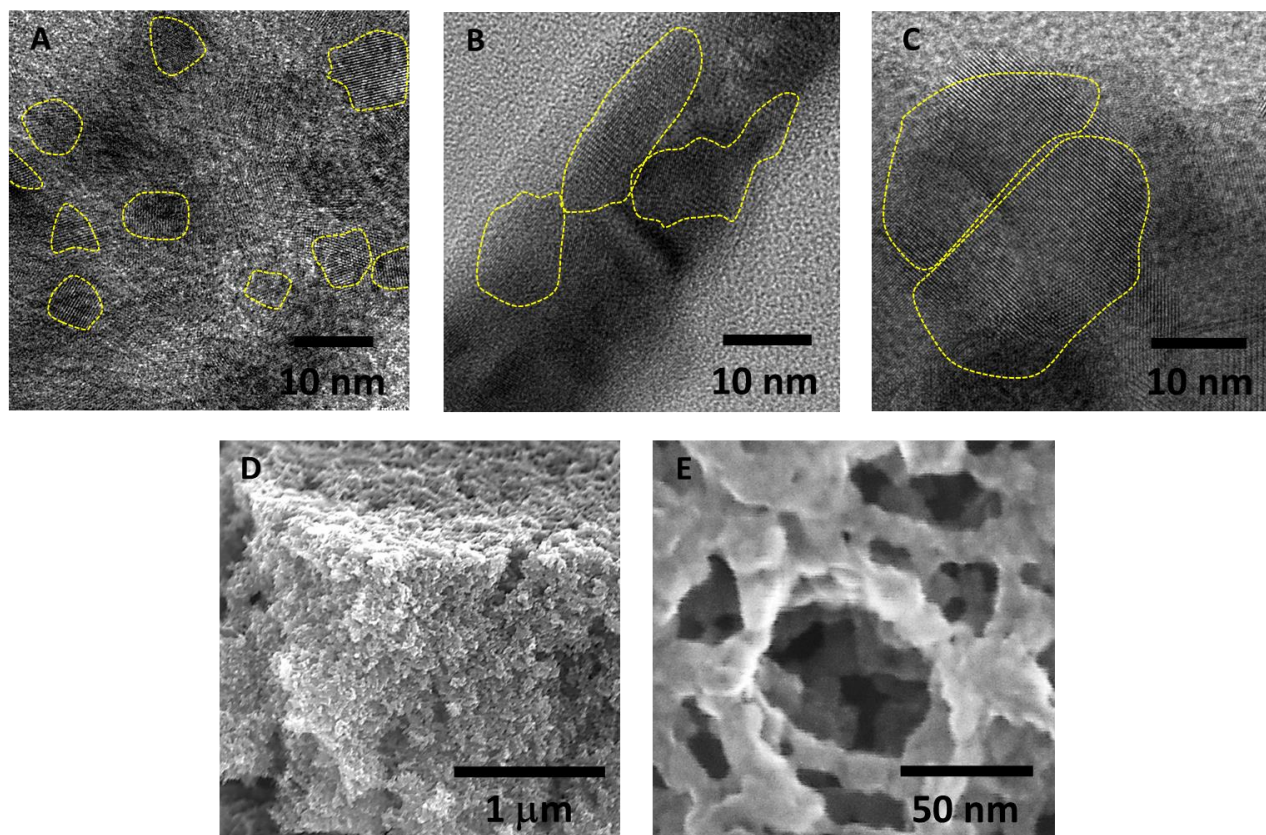


Figure 3. TEM images of the n-TiO₂ crystallites forming n-TiO₂ A. 20-nm-NWs, B. 30-nm-NWs, and C. 40-nm-NWs. The yellow dash lines indicate the presence of n-TiO₂ lattices and help visualize the size of crystallites. D. Cross-section and E. high-resolution SEM images of the mesoporous NW-based n-TiO₂ networks.

Increasing the amount of sacrificial polymer →

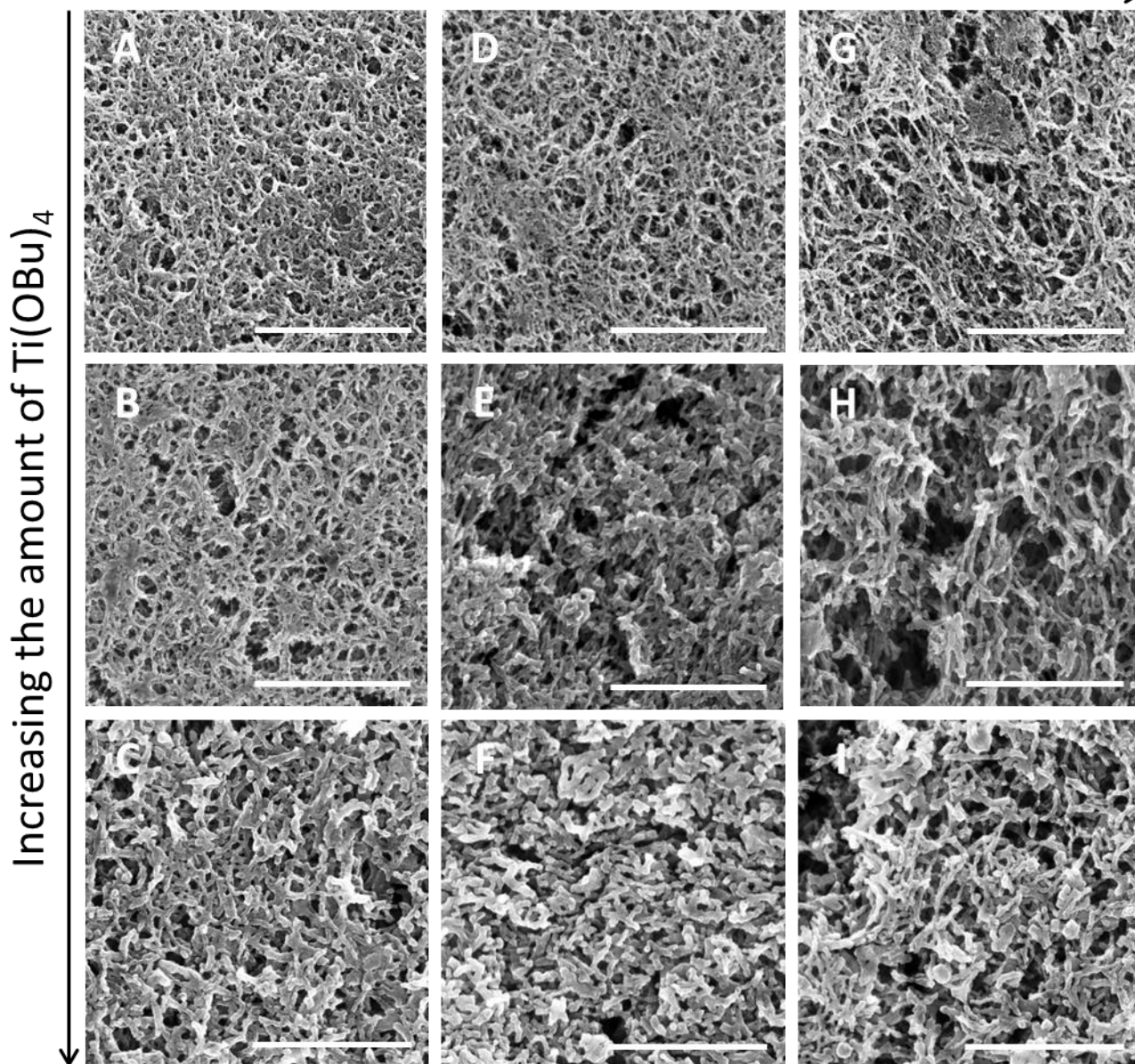


Figure 4. The SEM images of mesoporous NW-based n-TiO₂ networks. After 20-nm-NWs (Figure A, D, G), 30-nm-NWs (Figure B, E, H), and 40-nm-NWs (Figure C, F, I) are utilized as building-block-units and blended with sacrificial polymers in 50 wt.% (Figure A, B, C), 100 wt.% (Figure D, E, F), 200 wt.% (Figure G, H, I) of a-TiO₂ products, the surface morphologies of mesoporous semiconducting networks can be systematically controlled. The scale bars are all 1 μm.

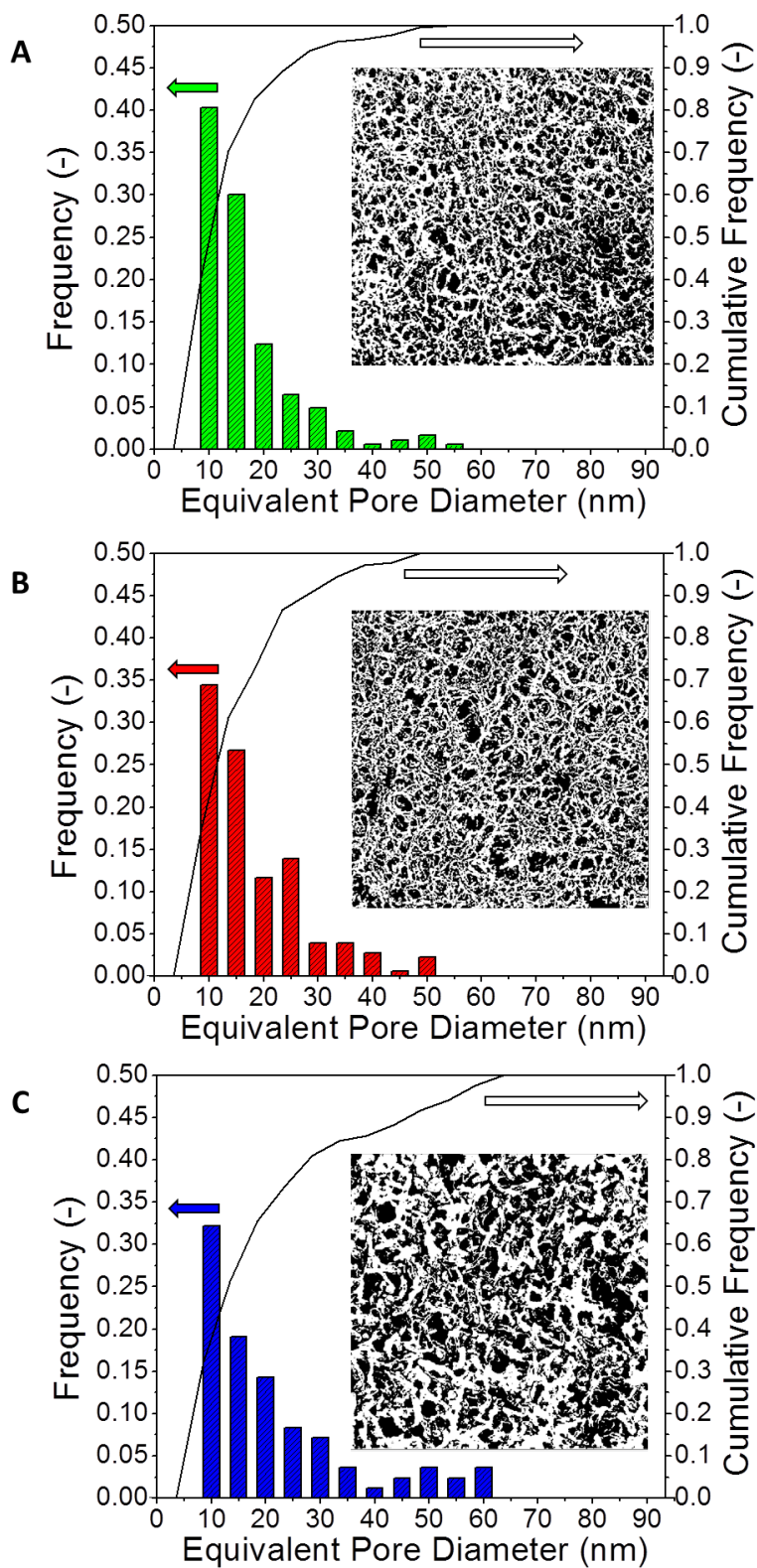


Figure 5. The pore size distribution calculated by the SEM images in Figure 4A-4C is shown in Figure 5A-5C. The average pore diameter of the mesoporous films increases

with increasing NW diameter; equivalent pore diameters sized 16.6 nm, 18.3 nm, and 21.2 nm is achieved using n-TiO₂ 20-, 30-, and 40-nm-NWs as building-block-units of mesoporous thin films, respectively.

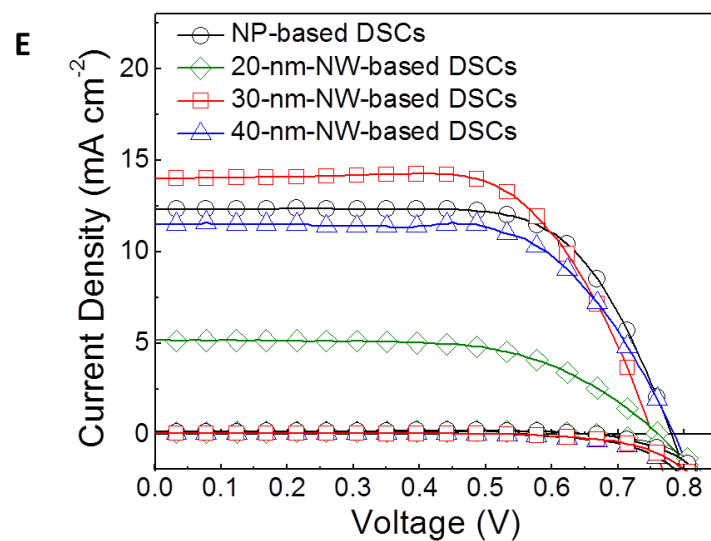
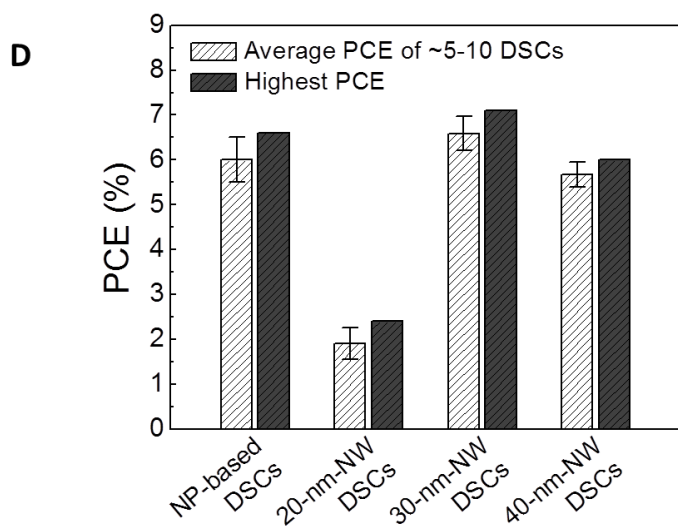
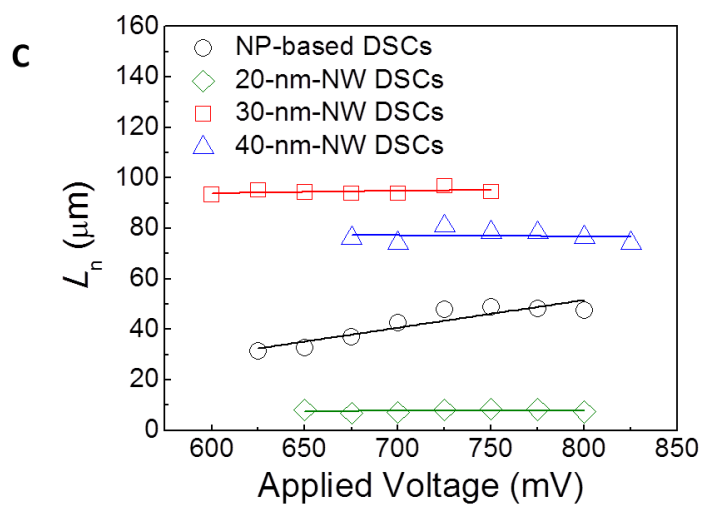
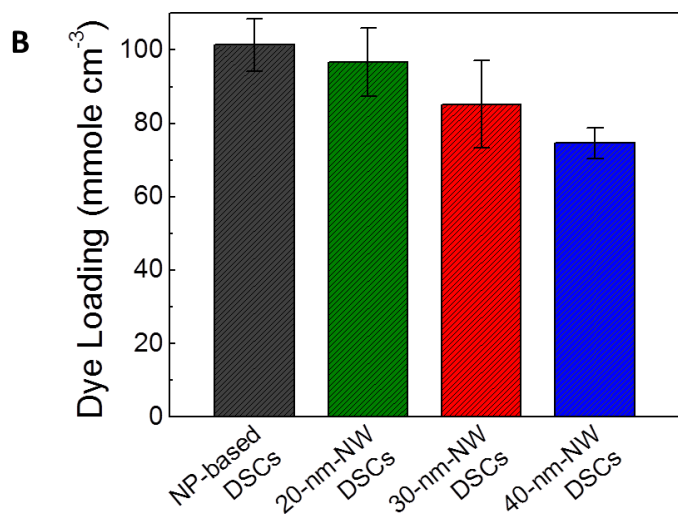
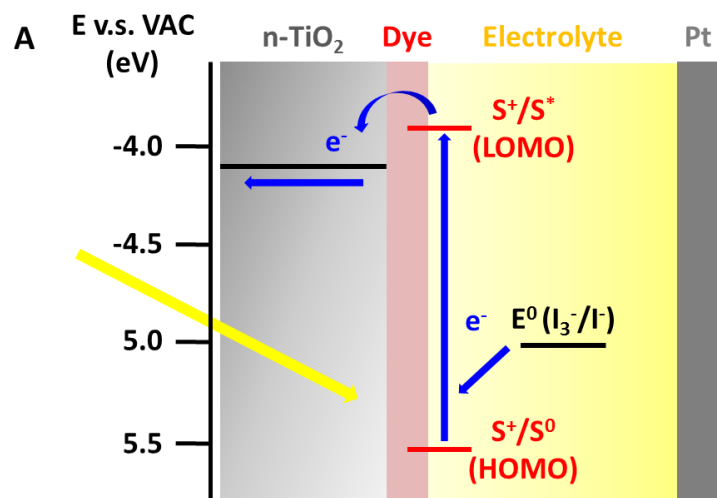


Figure 6. A. Dye loading of the NP-based and NW-based (including 20-nm-NW, 30-nm-NW, and 40-nm-NW) n-TiO₂ photoanodes. B. Diffusion length (L_n) analysis of the NP-based and NW-based (including 20-nm-NW, 30-nm-NW, and 40-nm-NW) n-TiO₂ photoanodes. C. Average and highest device performance among ~5-10 DSCs employing the NP-based and NW-based (including 20-nm-NW, 30-nm-NW, and 40-nm-NW) n-TiO₂ photoanodes. D. J - V curves of the most efficient DSC among ~5-10 devices employing the NP-based and NW-based (including 20-nm-NW, 30-nm-NW, and 40-nm-NW) n-TiO₂ photoanodes.

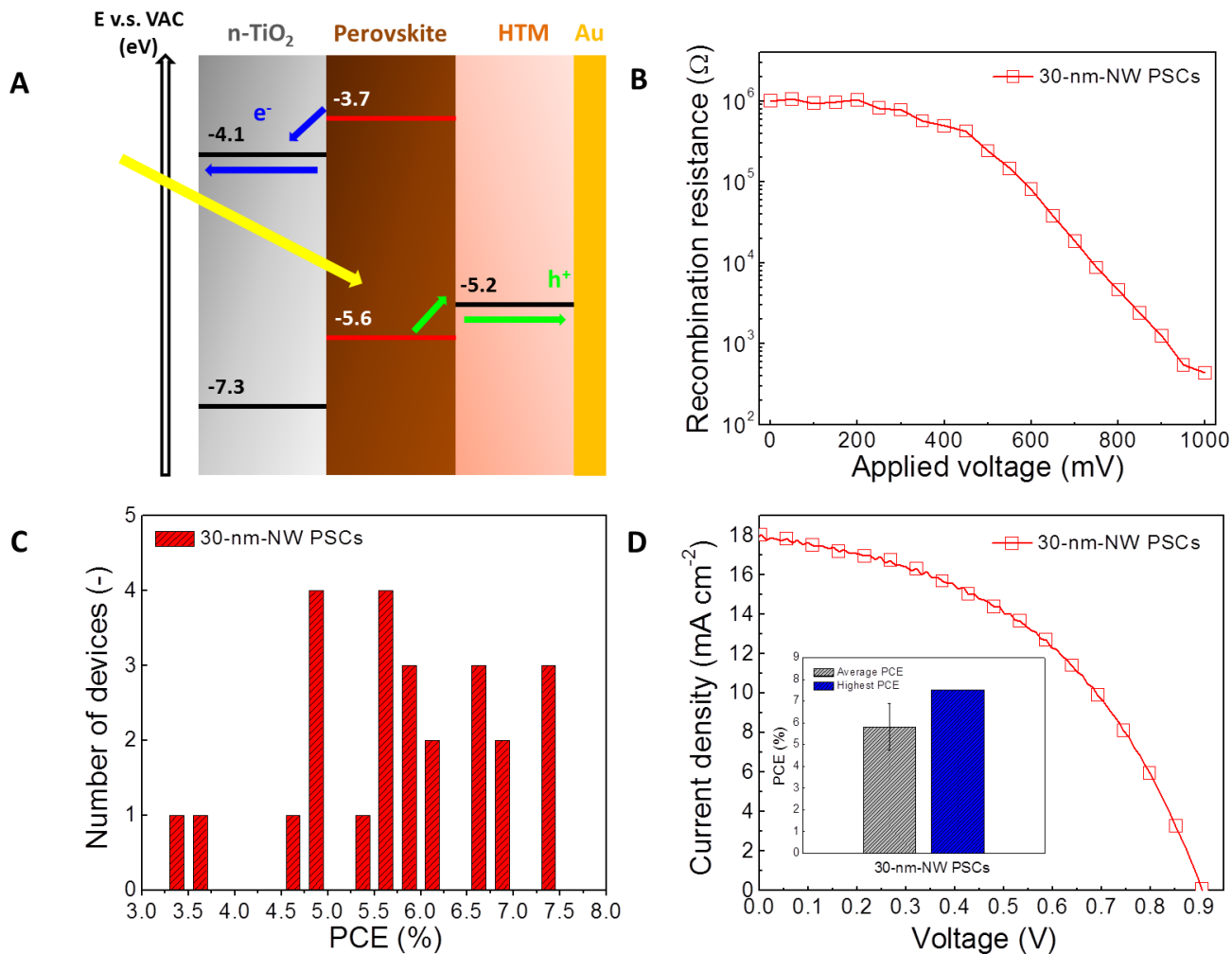
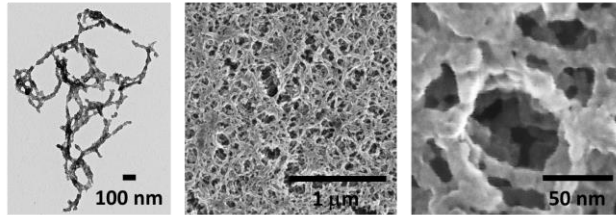
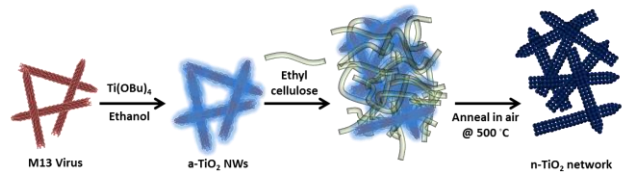


Figure 7. A. Resistance of electron recombination of the PSCs employing 30-nm-NW n-TiO₂ photoanodes. The resistances of electron recombination are determined from impedance measurements conducted in the dark. The Nyquist diagrams and the fitted lines are shown in Figure S4. B. *J-V* curves of the most efficient PSCs employing the NP-based and 30-nm-NW n-TiO₂ photoanodes and the related photovoltaic parameters listed in Table 1. The inset figure shows the average efficiency and highest performance of the PSCs employing 30-nm-NW n-TiO₂ photoanodes among multiple batches of PSCs (~25 devices in total). C. The static data of PCE distribution for multiple batches of PSCs (~25 devices in total) employing 30-nm-NW n-TiO₂ photoanodes. Each batch is around 8-10 devices, and three batches are conducted in total.

Table 1. Relevant solar cell parameters obtained from the DSCs in **Figure 6D** and the PSCs in **Figure 7C**.

| | V_{OC} [V] | J_{SC} [mA cm ⁻²] | FF [-] | PCE [%] | N719 loading [mmole cm ⁻²] | L_n @ 700 mV [μ m] | η_{COL} [%] |
|--------------|-----------------|------------------------------------|-----------|------------|---|------------------------------|---------------------|
| NP-based DSC | 0.777 | 12.3 | 0.69 | 6.6 | 101.4 | 37.1 | 93.9 |
| 20-nm-NW DSC | 0.761 | 5.2 | 0.61 | 2.4 | 96.7 | 6.8 | 51.2 |
| 30-nm-NW DSC | 0.750 | 14.0 | 0.67 | 7.1 | 85.3 | 93.9 | 99.5 |
| 40-nm-NW DSC | 0.785 | 11.5 | 0.66 | 6.0 | 74.6 | 76.1 | 99.3 |
| 30-nm-NW PSC | 0.910 | 17.8 | 0.46 | 7.5 | - | - | - |

TABLE OF CONTENTS/ABSTRACT GRAPHIC



M13 Virus-Enabled Synthesis of Titanium Dioxide Nanowires for Mesoporous Semiconducting Networks

Po-Yen Chen^{†,§}, Xiangnan Dang^{§,‡}, Matthew T. Klug^{§,1}, Noémie-Manuelle D. Courchesne^{†,§}, Jifa Qi^{§,‡}, Md Nasim Hyder^{†,§}, Angela M. Belcher^{§,‡,±,}, Paula T. Hammond^{†,§,*}*

[†]Department of Chemical Engineering, Massachusetts Institute of Technology,
Cambridge, MA 02139 (USA)

[§]The David H. Koch Institute for Integrative Cancer Research, Massachusetts Institute of
Technology, Cambridge, MA 02139 (USA)

[‡]Department of Materials Science and Engineering, Massachusetts Institute of
Technology, Cambridge, MA 02139 (USA)

¹Department of Mechanical Engineering, Massachusetts Institute of Technology,
Cambridge, MA 02139 (USA)

[±]Department of Biological Engineering, Massachusetts Institute of Technology,
Cambridge, MA 02139 (USA)

* Address correspondence to belcher@mit.edu and hammond@mit.edu

Supporting Information

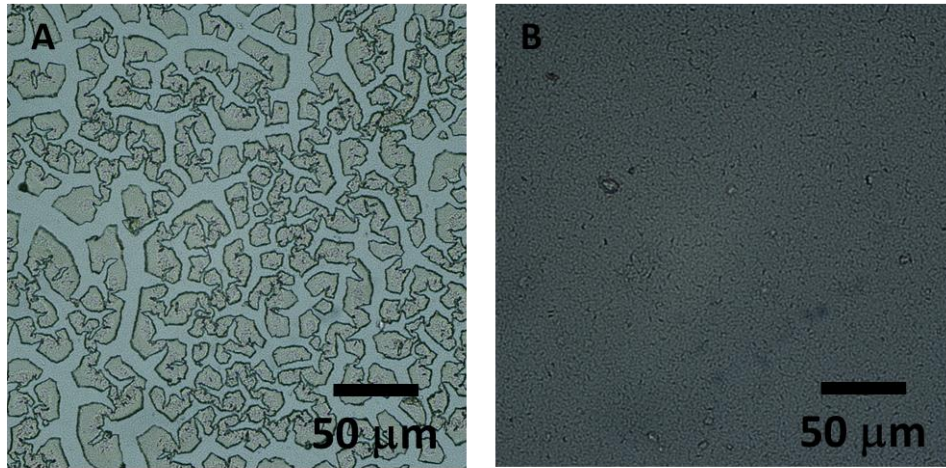


Figure S1. The microscopy images of the annealed NW-based n-TiO₂ films A. without and B. with employing the sacrificial polymers. The images indicate the sacrificial polymer helps prevent the formation of large crack during the annealing process.

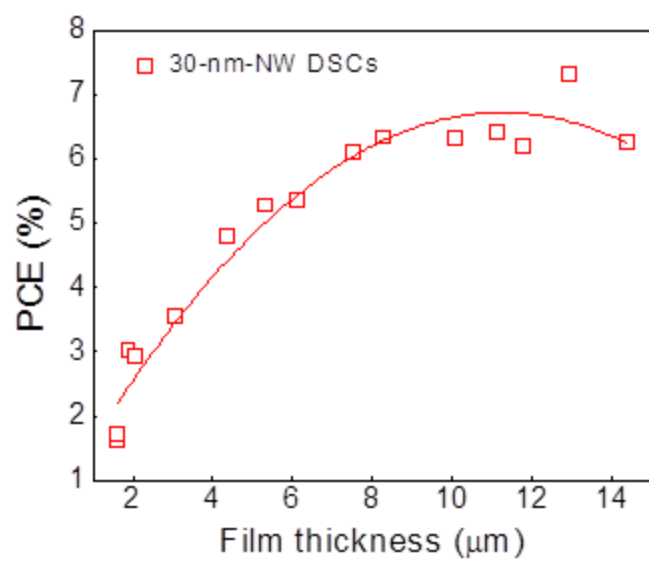


Figure S2 Dependence of PCEs on the thickness of DSC photoanodes.

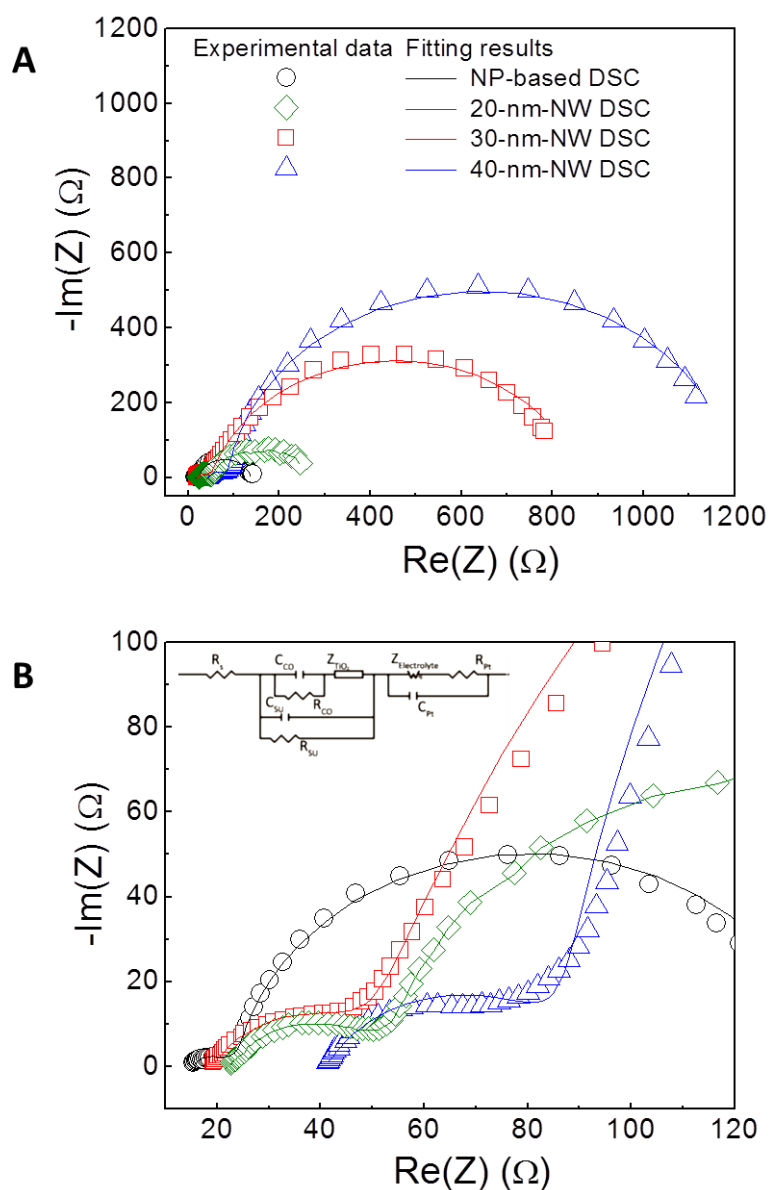


Figure S3. A. Nyquist diagrams of the EIS obtained under dark condition for different kinds of DSCs at 725 mV. B. The detailed EIS diagram at higher frequencies is shown. Both experimental data and fitted lines are shown. The inset is the equivalent circuit impedance model (transmission model) of DSCs. R_s : Ohmic series resistance of the cell. R_{CO} and C_{CO} : Contact resistance and capacitance at the interface between the conducting substrate and the TiO_2 photoanode film. R_{SU} and C_{SU} : Charge transfer resistance and double layer capacitance at the substrate/electrolyte interface. R_{Pt} and C_{PI} : Charge transfer resistance and double layer capacitance at the counter electrode-electrolyte interface. Z_{TiO_2} : transmission line impedance of the TiO_2 photoanode film consisting of the elements R_T (resistivity of electron transport in the photoanode film), R_{REC} (charge recombination resistance at the $\text{TiO}_2/\text{dye}/\text{electrolyte}$ interface), and C_μ (chemical

capacitance of the photoanode film). $Z_{\text{Electrolyte}}$: mass transport impedance at the counter electrode.

Calculation of Electron Diffusion Length (L_n) from Electrochemical Impedance Spectra (EIS)

The electron diffusion length, L_n , can be calculated from $L_n = L \times (R_{\text{REC}}/R_{\text{T}})^{1/2}$, where L is the film thickness, R_{REC} is electron recombination resistance, and R_{T} is electron transport resistance. R_{REC} and R_{T} were obtained by fitting the measured electrochemical impedance spectra to the transmission line model (shown in the inset of Figure S3B) with the Z-view software (v3.2b, Scribner Associates Inc). The transmission line component (Z_{TiO_2} in the inset of Figure S3B) in an equivalent circuit is often used to represent the interface resistance and capacitance for a porous structure, which is the case for the photoanodes of DSCs. During fitting the electrochemical impedance spectra to the transmission line model, the resistance and capacitance at the substrate/TiO₂ interface, and the substrate/electrolyte interface were assumed negligible due to good contact between substrate and TiO₂ and blocking layer of TiO₂. In Figure S3, electrochemical impedance spectra from each of three types of DSCs, measured at 725 mV, are shown in symbols. The fitted results are shown as solid lines. For more detailed information about fitting electrochemical impedance spectra to the transmission line model and extracting electron diffusion length from fitted electrochemical impedance spectra, refer references 21, 22, and 23.

Calculation of Electron Collection Efficiency (η_{COL}) from Electron Diffusion Length (L_n/L)

The electron collection efficiency is calculated by using the equation in reference 22:

$$\eta_{\text{COL}} = \frac{\left[-L\alpha \cosh\left(\frac{d}{L}\right) + \sinh\left(\frac{d}{L}\right) + L\alpha e^{-\alpha d} \right] L\alpha}{(1 - e^{-\alpha d}) \cdot [1 - L^2 \alpha^2] \cosh\left(\frac{d}{L}\right)}$$

where d is the thickness of the TiO₂ film, L is the electron diffusion length, and α is the extinction coefficient of dye sensitized TiO₂ film. The notation is different from that we used in the manuscript: we used L for the thickness of the TiO₂ film and L_n for the electron diffusion length. For the calculation, we assume αd equals to 1, indicating 90% of the incident light is absorbed. All L/d values were taken at a bias value of 725 mV, as shown in Figure 6B and Table 1.

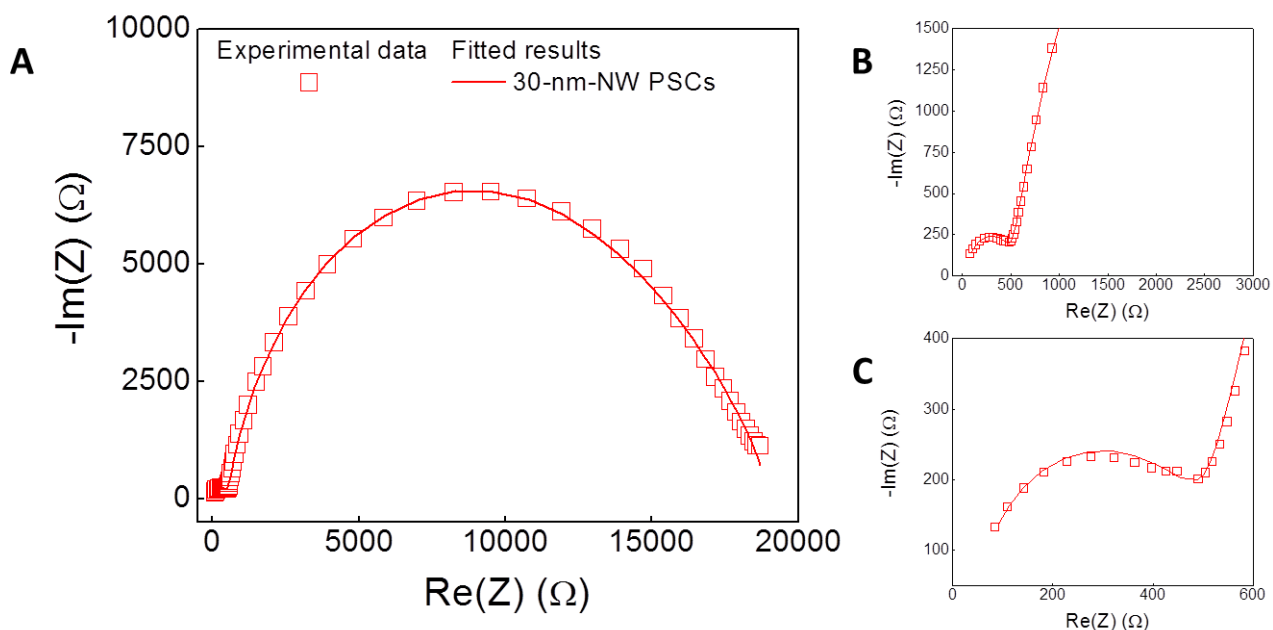


Figure S4. Nyquist diagrams of the EIS obtained under dark condition for PSCs employing the 30-nm-NW photoanodes. A-C are the Nyquist diagrams corresponding to the impedance spectra under dark conditions in the applied voltages at 700 mV. At high frequency (Figure S4C), the gold/HTM interface is similar to the interface between the liquid electrolyte and the counter electrode in DSCs (reference 29). The resistance at this interface remains almost the same over the whole applied voltage range, and the resistance slightly reduces at higher applied voltage, which is often observed in the literature (reference 30). Moreover, at intermediate frequency (Figure S4B), the straight characteristics of transmission line, which is normally observed in the nanostructured photoanodes, are seen. The transmission lines merge into the semicircles representing the recombination resistance at lower frequency. The solid lines are the fits by the reported models previously used in references 29, 30, 31, 32 and 33 for solid-state DSCs and PSCs.

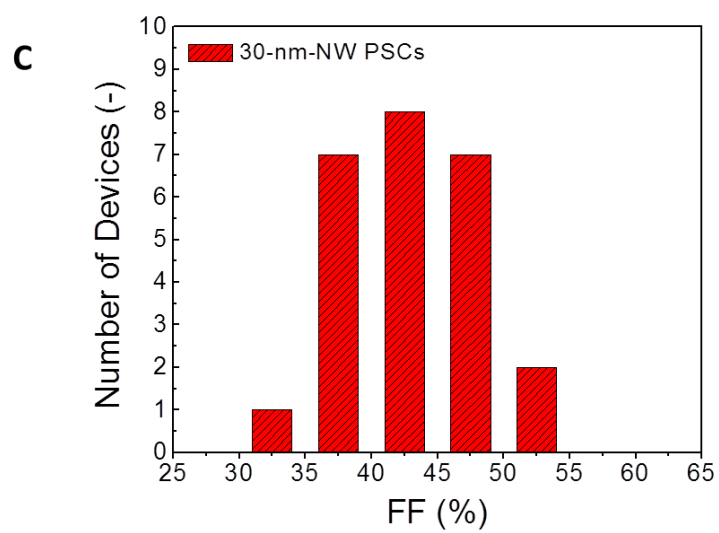
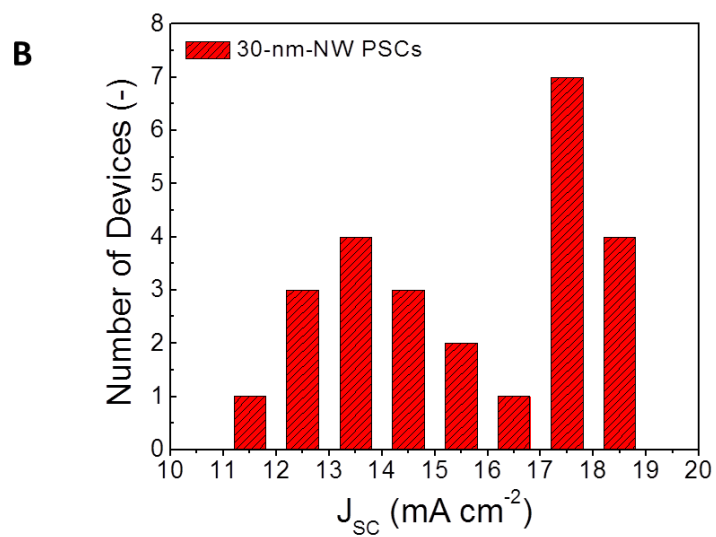
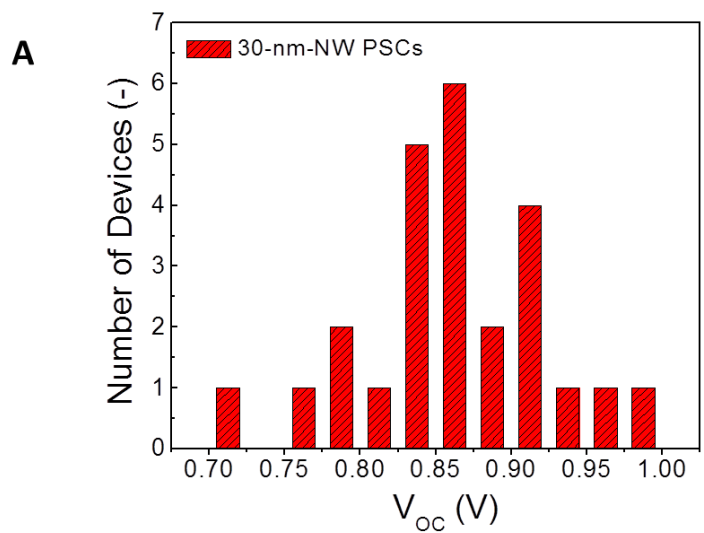


Figure S5. Static data of photovoltaic performance of PSCs employing the 30-nm-NW n-TiO₂ photoanodes. Histogram plots of solar cell performance parameters: A. V_{OC} , B. J_{SC} , and C. FF from multiple batches of CH₃NH₃PbI₃-sensitized TiO₂ photovoltaic devices (total of ~25 devices).

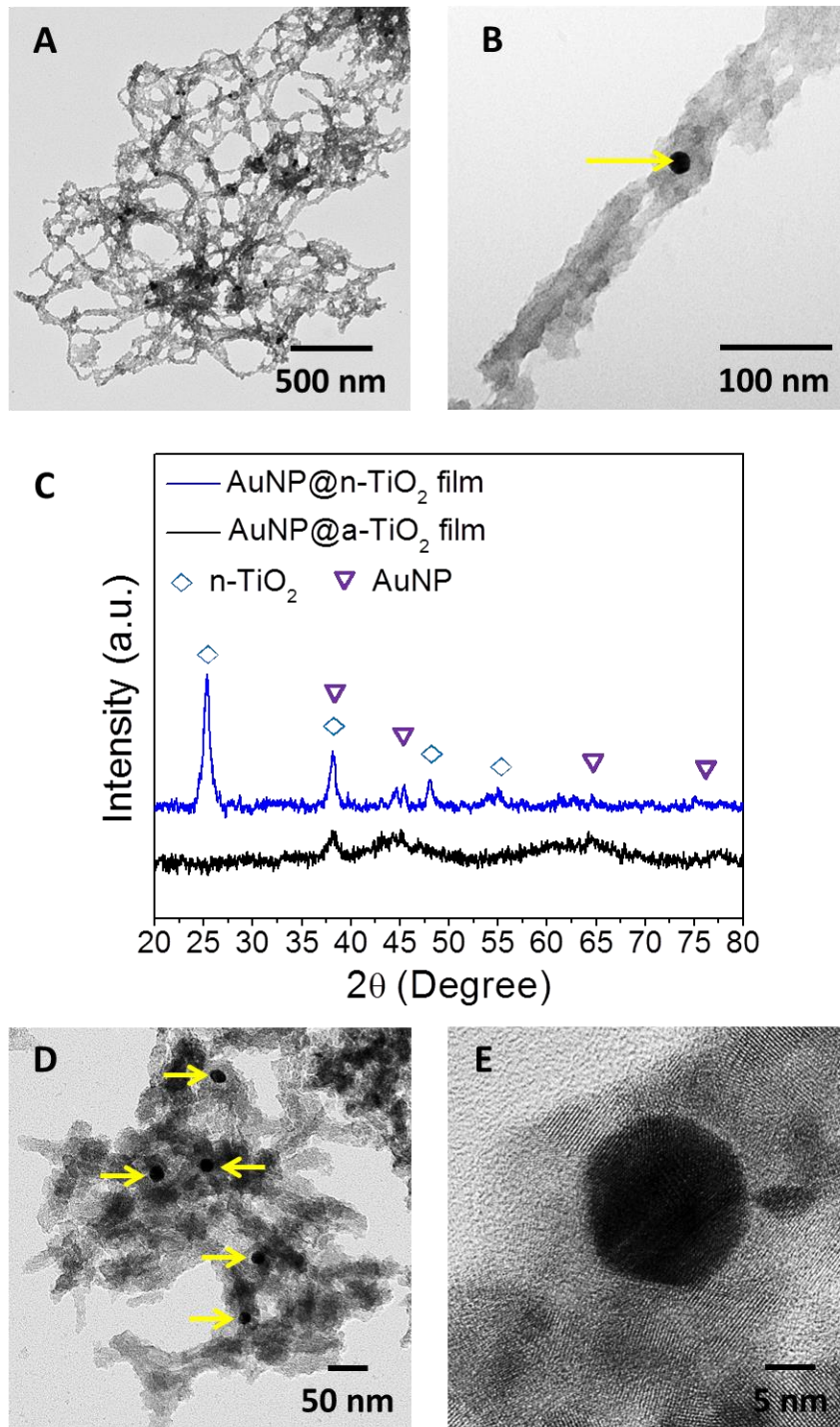


Figure S6. TEM images of A. B. the core-shell structures of AuNPs and n-TiO₂ NWs synthesized at -40 °C. C. XRD patterns of the AuNP@TiO₂ NWs before and after the annealing process. D. TEM image of the AuNP@n-TiO₂ NWs annealed at 500 °C. The yellow arrows point out the 20-nm AuNPs embedded in n-TiO₂ NWs. E. High resolution TEM image of AuNP and n-TiO₂ crystallites.